Theor Chem Account (2008) 120:437–445
DOI 10.1007/s00214-008-0420-0

REGULAR ARTICLE

Structure and electron paramagnetic resonance parameters of the manganese site of concanavalin A studied by density functional methods

Sandra Schinzel · Robert Müller · Martin Kaupp

Received: 27 September 2007 / Accepted: 5 February 2008 / Published online: 28 February 2008

Abstract The EPR parameters of the manganese site in the saccharide-binding protein concanavalin A have been studied by density functional methods, with an emphasis on metal (^{55}Mn) and ligand (^{1}H and ^{17}O) hyperfine couplings, in comparison with high-field EPR and ENDOR data. Results for gradient-corrected and hybrid functionals with different exact-exchange admixture have been compared with experiment for the ^{55}Mn and the ^{1}H ligand hyperfine coupling and have been predicted for ^{17}O hyperfine coupling based on comparison with experiment for the related $[Mn(H_2O)_6]^{2+}$. Appreciable exact-exchange admixture in the hybrid functional is needed to obtain an adequate spin-density distribution and thus near-quantitative agreement with experimental EPR parameters. The common use of experimental proton hyperfine coupling tensors together with the point-dipole approximation for determination of bond lengths is evaluated by explicit calculations.

Keywords Concanavalin A · Density functional theory · Electron paramagnetic resonance · *g*-Tensor · Hyperfine tensor · Manganese active site

1 Introduction

The saccharide-binding protein concanavalin A belongs to the large and ubiquitous plant lectin family [1]. The importance of these proteins is the ability to bind saccharides. Each member of the plant haemagglutinin has a unique saccharide specificity. However, many details of the biological role of these proteins are still unclear [1]. The metalloprotein concanavalin A of the Jack bean was the first saccharide-binding protein that has been characterized crystallographically [2,3]. It exhibits two metal ion binding sites, a transition-metal-binding site S1, which binds Mn^{2+}, Co^{2+}, Ni^{2+}, Zn^{2+} or Cd^{2+}, and a calcium-binding site S2, coordinating Ca^{2+} or Cd^{2+} [4]. The metal ions are responsible for stabilizing the binding site and for fixing the positions of amino acids that interact with sugar ligands [5].

Recently, the crystal structure of concanavalin A (Mn^{2+} on S1, Ca^{2+} on S2) and its bound water at 100 K was solved to an ultrahigh resolution (0.94 Å) based on synchrotron data [6]. The Mn^{2+} ion is surrounded by three carbonyl oxygen atoms, one nitrogen atom of histidine, and two water molecules in a slightly distorted octahedral coordination arrangement (Scheme 1). The Mn-O bond lengths in the plane containing the coordinating atoms of Asp1, Glu, Asp2, and H_2O (4) are nearly equal, whereas the bond lengths to His and H_2O (5) are significantly longer.

The first EPR study (35 GHz) on concanavalin A was reported in 1974, in which the Mn^{2+} spectrum of a single crystal was interpreted in terms of a spin Hamiltonian with an isotropic *g*-tensor ($g = 2.0009$), a nearly isotropic ^{55}Mn hyperfine tensor ($A_{||} = 264.3\,\text{MHz}$, $A_{\perp} = 256.2\,\text{MHz}$), and an axial zero-field splitting (ZFS) ($D = 0.02\,\text{cm}^{-1}$) [7,8].

Recently, Goldfarb et al. have investigated the frozen solution and the single crystal of concanavalin A by W-band (95 GHz) pulsed EPR and ^{1}H electron-nuclear double resonance spectroscopic techniques (ENDOR) [9]. HF-EPR and ^{1}H HF-ENDOR offer new opportunities for the investigation of paramagnetic transition metal complexes. In particular, for Mn^{2+} ($S = 5/2$, $I = 1/2$) it is better to measure the central transition $|-{}^{1}\!/_{2}, \text{m} > \; \rightarrow |{}^{1}\!/_{2}, \text{m} >$, thereby obtaining better resolution and a higher sensitivity. Contrary to X-ray crystallography, which is by far the most established and effective

---

Contribution to the Nino Russo Special Issue.

S. Schinzel · R. Müller · M. Kaupp (✉)
Institut für Anorganische Chemie, Universität Würzburg,
Am Hubland, 97074 Würzburg, Germany
e-mail: kaupp@mail.uni-wuerzburg.de

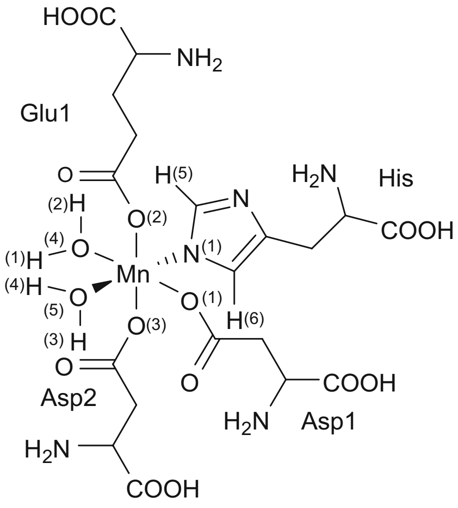

Scheme 1 A model of the Mn^{2+}-binding site S1, truncated after the first amino acid

method for determining the three-dimensional structure of proteins, ENDOR measurements on single crystals can provide information on the location of protons, when the metal center is paramagnetic [10,11]. Frozen solution results [9], from which the water proton positions could not be assigned uniquely, were refined in a single crystal study, and the atomic coordinates of the protons were calculated (within the point-dipole approximation) [11].

Our goal here is to confirm by quantum chemical calculations this type of structure determination by ENDOR, and to analyze the interrelations between electronic structure and EPR/ENDOR parameters for an experimentally well-investigated biological manganese site. To our knowledge, no theoretical studies on concanavalin A exist. Moreover, we use this well-defined biological system to evaluate the dependence of electronic structure and EPR parameters on a series of DFT exchange-correlation functionals. The yet unknown ^{17}O hyperfine couplings will be predicted. We want to identify the most suitable DFT methods to be applied also to computational studies on more complicated or less well-characterized biological Mn sites.

2 Theoretical formalism and computational details

The theoretical background of EPR parameters is covered in detail in various text books [12–17]. Here we summarize only the most relevant points.

2.1 g-Tensor calculations

The g-tensor will be provided as correction to the free-electron value g_e (in ppt, i.e. in units of 10^{-3})

$$g = g_e 1 + \Delta g, \tag{1}$$

with $g_e = 2.002319$. Up to the level of second-order perturbation theory based on the Breit–Pauli Hamiltonian, the g-shift Δg consists of three terms:

$$\Delta g = \Delta g^{\mathrm{SO/OZ}} + \Delta g^{\mathrm{RMC}} + \Delta g^{\mathrm{GC}}, \tag{2}$$

of which the "paramagnetic" second-order spin-orbit/orbital Zeeman cross term, $\Delta g^{\mathrm{SO/OZ}}$, dominates (except for extremely small Δg values) [12]. The relativistic mass correction term Δg^{RMC} and the one-electron part of the gauge correction term Δg^{GC} are also included in our implementation [18,19] (see also refs. [20,21] for related implementations).

2.2 Hyperfine tensor calculations

In the usual nonrelativistic first-order approximation, isotropic hyperfine splittings $A_{\mathrm{iso}}(N)$ correspond to the Fermi-contact term A^{FC}:

$$\mathbf{A}_{\mathrm{iso}}(N) = \mathbf{A}^{\mathrm{FC}} = \frac{4\pi}{3} \beta_{\mathrm{e}} \beta_{\mathrm{N}} g_{\mathrm{e}} g_{\mathrm{N}} \langle S_Z \rangle^{-1} \sum_{\mu,\nu} P^{\alpha-\beta}_{\mu,\nu} \times \left\langle \varphi_\mu \left| \delta\left(\mathbf{R}_{\mathrm{N}}\right) \right| \varphi_\nu \right\rangle. \tag{3}$$

Here β_{e} is the Bohr magneton, β_{N} the nuclear magneton, g_{N} is the g-value of nucleus N, $\langle S_Z \rangle$ is the expectation value of the z-component of the total electronic spin, $P^{\alpha-\beta}_{\mu,\nu}$ is the spin density matrix, and the summation runs over all occupied molecular orbitals. The components $A^{\mathrm{dip}}_{ij}(N)$ of the anisotropic tensor are given by

$$A^{\mathrm{dip}}_{ij}(N) = \frac{1}{2} \beta_{\mathrm{e}} \beta_N g_{\mathrm{e}} g_N \langle S_Z \rangle^{-1} \sum_{\mu,\nu} P^{a-\beta}_{\mu,\nu} \times \left\langle \varphi_\mu \left| \mathbf{r}_N^{-5} \left(\mathbf{r}_N^2 \delta_{ij} - 3 \mathbf{r}_{N,i} \mathbf{r}_{N,j} \right) \right| \varphi_\nu \right\rangle, \tag{4}$$

where $r_N = r - R_N$ (R_N is the position vector of nucleus N). In the rest of this section, we will refer to the metal hyperfine interaction and omit subscript N. The second-order perturbation treatment of Refs. [22,23] is used to compute spin-orbit (SO) corrections to the hyperfine tensor (in this work, the corrections are only relevant for the metal HFC). At the coupled-perturbed Kohn–Sham level, the dominant SO correction term arises as a second-order cross term between the one- and two-electron SO Hamiltonian H^{SO} and the perturbed Fock operator F'

$$\mathbf{A}^{SO-I}_{K,uv} = \frac{1}{2} \alpha^4 g_e \gamma_K \frac{1}{2\langle S_Z \rangle} \times \left[\sum_{k}^{\mathrm{occ}(\alpha)} \sum_{a}^{\mathrm{virt}(\alpha)} \frac{\left\langle \psi_k^\alpha \middle| h_u^{SO} \middle| \psi_a^\alpha \right\rangle \left\langle \psi_a^\alpha \middle| F'_v \middle| \psi_k^\alpha \right\rangle}{\varepsilon_k^\alpha - \varepsilon_a^\alpha} - \sum_{k}^{\mathrm{occ}(\beta)} \sum_{a}^{\mathrm{virt}(\beta)} \frac{\left\langle \psi_k^\beta \middle| h_u^{SO} \middle| \psi_a^\beta \right\rangle \left\langle \psi_a^\beta \middle| F'_v \middle| \psi_k^\beta \right\rangle}{\varepsilon_k^\beta - \varepsilon_a^\beta} \right] \tag{5}$$

where α is the fine-structure constant, γ_K the gyromagnetic ratio of the nucleus, h_{SO} is explained below, F' is the perturbed Fock operator, with $F'_v = (\ell_v/r^3) - \frac{2}{\alpha} a_0 \sum_{k=1}^{n/2} K'_v$, where $\left(\ell_v/r^3\right)$ is the paramagnetic nuclear-spin electron-orbit (PSO) operator, K'_v is a component of the response exchange operator, and a_0 is the weight of HF exchange depending on the specific hybrid functional used (see Ref. [24] for a related simultaneous CPKS implementation, and also Refs. [22,23] for references to earlier work). ψ^σ and ε^σ are spin-polarized Kohn–Sham orbitals and orbital energies, respectively. GGA or LDA functionals lead to an uncoupled DFT (UDFT) treatment for this second-order term ($a_0 = 0$).

2.3 Computational details

Initial coordinates have been taken from the 0.94 Å resolution synchrotron data, deposited in the Protein Data Bank (PDB entry 1NLS; cf. Fig. 1) [6]. Keeping the heavy-atom positions fixed, the hydrogen positions were then optimized, except for those of the two water molecules, for which optimized distances (0.976 Å) and angles (106.5°) for a coordinated water molecule in the $[\mathrm{Mn(H_2O)_6}]^{2+}$ complex were applied (Model "dist. X-ray"). The optimization was carried out with the Turbomole 5.8 code [25] at B3LYP [26,27] DFT level with SVP basis sets [28] using unrestricted Kohn–Sham wavefunctions. Attempts of a full structure optimization resulted in a breakdown of the coordination sphere (one ligand was expelled), indicating that constraints due to the protein environment have to be taken into account (in particular, there are bridges between different amino acids that are probably structurally relevant but not included in the computational model used for optimization). When keeping the heavy-atom positions fixed, the smaller computational model (Fig. 1) and a more extended model corresponding to the atoms shown in Scheme 1 provided virtually identical spin-density distributions and EPR parameters. We will therefore in the following concentrate on the smaller model. In addition to the structure derived from the X-ray data, we investigated also a model, in which the metal–ligand distances were adjusted to reproduce the Mn–H distances from ENDOR data [9] (Model "dist. ENDOR"), while keeping angles and bond lengths within the ligands fixed to the same values as in the first model.

Unrestricted Kohn–Sham single-point calculations were performed with Gaussian03 [29] using a 9s7p4d basis set for manganese (specifically designed for hyperfine calculations [27,28,30,31]) and flexible IGLO-III [32,33] basis sets for the ligand atoms. The following DFT exchange-correlation functionals were compared: the GGA functionals (a) BP86 [34,35] and (b) BLYP [26,27], the hybrid functionals (c) B3LYP [26,27] with 20% exact exchange and (d) BHLYP [26,36] with 50% exact exchange, as well as the user-defined hybrid functionals (e) B60LYP with 60% exact exchange (40% $E_{\mathrm{X}}^{\mathrm{Slater}}$ and 40% $\Delta E_{\mathrm{x}}^{\mathrm{B88}}$ and $E_{\mathrm{c}}^{\mathrm{LYP}}$) and (f) B70LYP with 70% exact exchange (30% $E_{\mathrm{X}}^{\mathrm{Slater}}$ and 30% $\Delta E_{\mathrm{x}}^{\mathrm{B88}}$ and $E_{\mathrm{c}}^{\mathrm{LYP}}$).

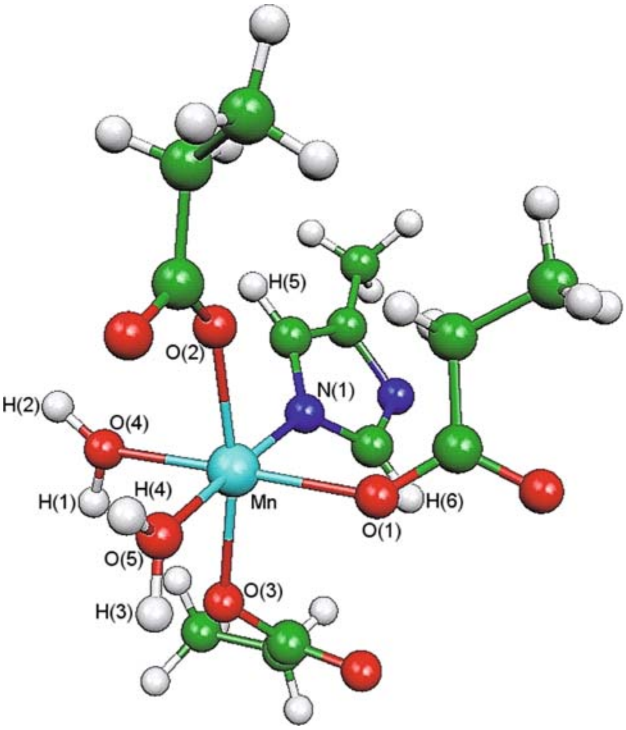

Fig. 1 Structure and atom labels of concanavalin A

The unrestricted Kohn–Sham orbitals were transferred to the MAG-Respect property package [37] by suitable interface routines. The atomic mean-field approximation (AMFI) [38,39] has been used to compute the matrix elements of the spin-orbit (SO) operator. In g-tensor calculations, a common gauge at the metal center was employed. Differences between calculations with the IGLO-III basis and IGLO-II-based results are very small for ^{1}H HFC (<0.1 MHz), suggesting that the ligand basis set is essentially converged. The Fermi-contact contributions to the ^{55}Mn HFC change by 2 MHz, suggesting that there is a very slight shift of spin density. We will exclusively report the IGLO-III-based results.

The dielectric constant of a protein is not very high ($\varepsilon \approx 4$). Therefore, solvent effects were evaluated by Kohn–Sham single point calculations using the polarizable continuum model (PCM) and the BHLYP functional in chloroform ($\varepsilon = 4.9$). The ^{1}H HFC differs only slightly between gas phase and solvent calculations (<0.1 MHz). A small influence is observed for the Fermi-contact term $\mathrm{A^{FC}}$ for the ^{55}Mn HFC (gas phase: −196.0 MHz, $\mathrm{CHCl_3}$: −199.8 MHz). In the following only the gas phase calculations will be discussed.

Table 1 Mulliken atomic spin densities and $\langle S^2 \rangle$ expectation values in the concanavalin A model

	Mn	O(1)	O(2)	O(3)	O(4)	O(5)	N(1)
BP86	4.901	0.014	−0.006	−0.003	−0.027	−0.019	−0.035
BLYP	4.786	0.031	0.006	0.012	−0.020	−0.009	−0.017
B3LYP	4.905	0.014	0.003	0.002	−0.007	−0.005	−0.015
BHLYP	4.929	0.009	0.004	0.002	−0.001	0.000	−0.008
B-60LYP	4.930	0.009	0.005	0.003	0.000	0.001	−0.006
B-70LYP	4.920	0.012	0.006	0.002	0.002	0.003	−0.002

	H(1)	H(2)	H(3)	H(4)	H(5)	H(6)	$\langle S^2 \rangle$
BP86	0.043	0.034	0.022	0.016	−0.001	0.001	8.758
BLYP	0.055	0.047	0.026	0.017	0.000	0.001	8.760
B3LYP	0.018	0.015	0.012	0.009	0.000	0.001	8.754
BHLYP	0.009	0.007	0.006	0.005	0.000	0.000	8.753
B-60LYP	0.007	0.006	0.005	0.004	0.000	0.000	8.753
B-70LYP	0.006	0.005	0.005	0.004	0.000	0.000	8.753

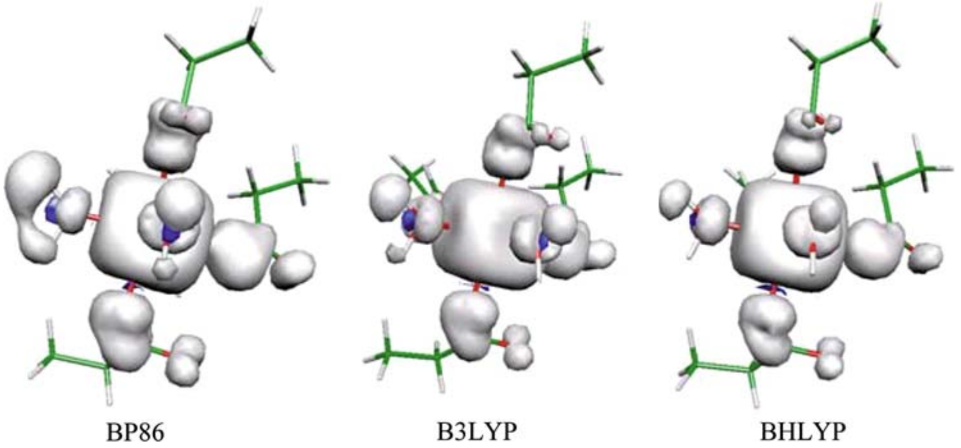

Fig. 2 Spin-density distribution. Isosurfaces ±0.0005 a.u

3 Results and discussion

Goldfarb et al. have carried out several W-band (95 GHz) pulsed EPR and electron-nuclear double resonance (ENDOR) studies on concanavalin A in frozen solution and in a single crystal [9,11,40–42]. ^{1}H ENDOR indicated all protons to have axially symmetric hyperfine tensors. The two imidazole protons, located 3.56 Å from Mn^{2+}, are magnetically equivalent, but the four water protons are magnetically inequivalent, located at distances between 2.67 and 3.24 Å.

3.1 Spin density analysis

As the computed EPR/ENDOR parameters depend decisively on the quality of the spin-density distribution, Table 1 provides Mulliken atomic spin densities (atomic spin densities from natural population analyses are very similar) obtained with different functionals. Spin-density isosurface plots with a subset of three functionals are shown in Fig. 2.

Spin contamination of the Kohn–Sham wavefunction is small, even with large exact-exchange admixtures (cf. $\langle S^2 \rangle$ expectation values in Table 1). In fact, the spin contamination decreases even somewhat with more exact exchange, which is probably indirectly due to the enhanced ionicity of the metal–ligand bonds. Exact-exchange admixture has usually three effects on the spin-density distribution in transition-metal complexes [30,31,43]: (a) the metal–ligand bond becomes more ionic (self-interaction errors tend to render the bonds too covalent at LDA or GGA level) [19,31,43–46], (b) valence-shell spin polarization across covalent bonds is enhanced, leading often to larger spin contamination [31], and (c) core-shell spin polarization at the metal center is also enhanced (improved). While the latter effect is important for the metal hyperfine coupling [31] (see below), the two former trends may counteract each other [45,47]: the increased ionicity may actually decrease the tendency towards valence-shell spin polarization. This seems to be the case here. The enhanced bond ionicity is reflected in an increase of spin density at the metal center and less spin density on the ligand atoms (Table 1, Fig. 2).

Independent of the functional and of details of the spin-density distribution, an assignment to an electronic structure of a high-spin $Mn^{2+}(d^5)$ system is obtained at all computational levels. The manganese spin density is close to the formally expected five unpaired spins (Table 1). The coordinated histidine nitrogen atom exhibits negative spin density due to spin polarization. At BP86 level, negative spin density is found also for four oxygen atoms in the first coordination sphere. This is reduced to just one oxygen atom at BHLYP level (Table 1). Above 50% exact exchange, only the negative spin density on nitrogen remains. Thus, in contrast to many other cases [30,31,45], obviously spin polarization becomes less important here with more exact exchange, due to less delocalization of spin density upon the ligands. Delocalized positive spin density is found particularly at the water and imidazole protons.

3.2 The g-tensor

An isotropic g-tensor with $g_{\mathrm{iso}} = 2.0009 \pm 0.0004$ (the uncertainty may also be considered as an upper limit for the g-anisotropy) was measured (EPR study at 35 GHz) [8]. This is the expected situation for a high spin d^5Mn^{2+} complex. Our calculations (Table 2) confirm the very small g-shifts and extremely small anisotropy. Larger exact-exchange admixture reduces g_{iso} somewhat and thereby improves agreement with experiment.

3.3 ^{55}Mn hyperfine coupling constant

Isotropic ^{55}Mn hyperfine data are available from Q- and W-band EPR studies [8,9] and are compared to our computations in Table 3 (HFC anisotropy is available from Q-band single-crystal measurements [7,8]). The isotropic coupling constant A_{iso} in such systems depends appreciably on exact-exchange admixture, due to an enhancement of (overall negative) core–shell spin polarization contributions to the spin density at the nucleus [31,48] (and due to generally more spin density on manganese, see above). This renders the couplings more negative and improves agreement with the experimental data [8,9] (Table 3). The negative sign of A_{iso} has been confirmed experimentally [42,49]. The extremely small HFC anisotropy found [7,8] is also confirmed by the calculations. It reflects the rather isotropic spin-density distribution in a high-spin Mn^{2+} system.

Table 2 g-Shift components (in ppt) and absolute g-values of the concanavalin A model

	Δg_{iso}	Δg_{11}	Δg_{22}	Δg_{33}
BP86	0.1	0.0	0.0	0.2
	(2.0024)	(2.0023)	(2.0023)	(2.0025)
BLYP	0.1	−0.1	0.0	0.3
	(2.0024)	(2.0022)	(2.0023)	(2.0026)
B3LYP	−0.2	−0.3	−0.2	−0.2
	(2.0021)	(2.0020)	(2.0021)	(2.0021)
BHLYP	−0.4	−0.5	−0.4	−0.4
	(2.0019)	(2.0018)	(2.0019)	(2.0019)
B-60LYP	−0.5	−0.5	−0.5	−0.4
	(2.0018)	(2.0018)	(2.0018)	(2.0019)
B-70LYP	−0.5	−0.5	−0.5	−0.4
	(2.0018)	(2.0018)	(2.0018)	(2.0019)
Exp.[a]	-1.4 ± 0.4			
	(2.0009 ± 0.0004)			

Absolute g-values in parentheses

[a] From 35 GHz EPR measurements on a single crystal of Mn^{2+}, Ca^{2+}-concanavalin A [8]

Table 3 Computed and experimental ^{55}Mn HFC tensors (in MHz)

	First-order				A^{SO}	Total A-tensor	
	A^{FC}	A_{11}^{dip}	A_{22}^{dip}	A_{33}^{dip}	A^{PC}	A_{iso}	$\langle S^2 \rangle$
BP86	−140.2	−1.2	−0.3	1.5	−3.1	−143.3	8.758
BLYP	−122.0	−2.1	0.0	2.2	−3.1	−125.1	8.760
B3LYP	−155.6	−0.5	−0.2	0.7	−2.7	−158.3	8.754
BHLYP	−196.0	−0.6	0.0	0.6	−2.2	−198.2	8.753
B-60LYP	−208.1	−0.7	0.0	0.6	−2.0	−210.1	8.753
B-70LYP	−224.6	−0.9	0.1	0.7	−1.8	−226.3	8.753
Exp.[a]		−2.7	−2.7	5.4		−258.9	
Exp.[b]						−262.5	

[a] From 35 GHz EPR measurements on a single crystal of Mn^{2+}, Ca^{2+}-concanavalin A [8]

[b] From 95 GHz ENDOR [42]

Table 3 also provides SO corrections to the hyperfine tensor. SO contributions have previously been found to be very important already for 3d metals [23,24,47]. Here they are rather small compared to the nonrelativistic A_{iso} (FC), again in agreement with the d^5 configuration (for an O_h symmetrical high-spin d^5 system with $^6A_{1g}$ ground state, SO effects would vanish exactly).

3.4 ^{1}H hyperfine coupling constants

The ^{1}H HFCs were computed for two different structures (Table 4): (a) after DFT optimization of the hydrogen positions (except for the water protons, for which standard water structure parameters were used; see Sect. 2), and (b) after

Table 4 Computed and experimental ^{1}H HFC tensors (in MHz)

	A_{iso}	A^{FC}	$A_{11}^{\mathrm{dip}}/A_{22}^{\mathrm{dip}}$	A_{33}^{dip}	A'^{a}
H(1)					
dist. X-ray[b] 2.89 Å					
BP86	3.7	3.7	−3.2/−3.1	6.3	
BLYP	4.4	4.4	−3.2/−3.2	6.3	
B3LYP	2.4	2.4	−3.3/−3.2	6.4	
BHLYP	1.6	1.6	−3.3/−3.1	6.5	6.4
B-60LYP	1.5	1.5	−3.3/−3.1	6.5	
B-70LYP	1.4	1.4	−3.3/−3.1	6.5	
dist. ENDOR[c] 2.67 Å					
BP86	1.6	1.6	−4.0/−3.8	7.9	
BLYP	1.7	1.7	−4.1/−3.8	7.8	
B3LYP	0.9	0.9	−4.2/−3.9	8.0	
BHLYP	0.5	0.5	−4.2/−3.9	8.1	8.1
B-60LYP	0.4	0.4	−4.2/−3.9	8.1	
B-70LYP	0.4	0.4	−4.2/−3.9	8.1	
Exp.[d]	0.1		−4.2	8.2	
Exp.[e]	0.1		−4.0	8.0	
H(2)					
dist. X-ray[b] 2.85 Å					
BP86	2.3	2.3	−3.3/−3.3	6.6	
BLYP	2.7	2.7	−3.3/−3.3	6.6	
B3LYP	1.7	1.7	−3.4/−3.3	6.7	
BHLYP	1.2	1.2	−3.5/−3.3	6.8	6.8
B-60LYP	1.1	1.1	−3.5/−3.3	6.8	
B-70LYP	1.0	1.0	−3.5/−3.3	6.8	
dist. ENDOR[c] 2.99 Å					
BP86	5.0	5.0	−3.0/−2.8	5.8	
BLYP	5.5	5.5	−3.0/−2.9	5.8	
B3LYP	3.4	3.4	−3.0/−2.9	5.9	
BHLYP	2.6	2.6	−3.0/−2.9	5.9	5.9
B-60LYP	2.4	2.4	−3.0/−2.9	5.9	
B-70LYP	2.3	2.3	−3.0/−2.9	5.9	
Exp.[d]	0.1		−3.0	6.0	
Exp.[e]	0.8		−3.5	7.0	
H(3)					
dist. X-ray[b] 2.97 Å					
BP86	2.2	2.2	−3.0/−2.9	5.9	
BLYP	2.5	2.5	−3.0/−2.9	5.9	
B3LYP	1.6	1.6	−3.0/−2.9	6.0	
BHLYP	1.2	1.2	−3.1/−2.9	6.0	5.9
B-60LYP	1.1	1.1	−3.1/−2.9	6.0	
B-70LYP	1.0	1.0	−3.1/−2.9	6.0	
dist. ENDOR[c] 2.76 Å					
BP86	0.2	0.2	−3.8/−3.4	7.2	
BLYP	0.2	0.2	−3.8/−3.4	7.1	
B3LYP	0.1	0.1	−3.9/−3.5	7.3	
BHLYP	−0.1	−0.1	−3.9/−3.5	7.4	7.4
B-60LYP	−0.1	−0.1	−3.9/−3.5	7.4	
B-70LYP	−0.1	−0.1	−3.9/−3.5	7.4	
Exp.[d]	0.0		−3.75	7.5	
Exp.[e]	0.4		−3.9	7.8	
H(4)					
dist. X-ray[b] 2.93 Å					
BP86	1.5	1.5	−3.1/−3.0	6.0	
BLYP	1.7	1.7	−3.1/−2.9	6.0	
B3LYP	1.2	1.2	−3.2/−3.0	6.2	
BHLYP	0.9	0.9	−3.2/−3.0	6.2	6.3
B-60LYP	0.9	0.9	−3.2/−3.0	6.2	
B-70LYP	0.8	0.8	−3.2/−3.0	6.2	
dist. ENDOR[c] 3.24 Å					
BP86	2.4	2.4	−2.3/−2.2	4.5	
BLYP	2.7	2.7	−2.3/−2.2	4.6	
B3LYP	2.0	2.0	−2.4/−2.3	4.7	
BHLYP	1.6	1.6	−2.4/−2.3	4.7	4.6
B-60LYP	1.5	1.5	−2.4/−2.3	4.7	
B-70LYP	1.5	1.5	−2.4/−2.3	4.7	
Exp.[d]	0.6		−2.7	5.4	
Exp.[e]	0.4		−2.5	5.0	
H(5)					
dist. X-ray[b] 3.39 Å					
BP86	0.2	0.2	−2.0/−1.9	3.8	
BLYP	0.2	0.2	−2.0/−1.8	3.8	
B3LYP	0.1	0.1	−2.0/−1.9	3.9	
BHLYP	0.1	0.1	−2.0/−1.9	3.9	4.1
B-60LYP	0.1	0.1	−2.0/−1.9	4.0	
B-70LYP	0.1	0.1	−2.0/−1.9	4.0	
dist. ENDOR[c] 3.56 Å					
BP86	0.1	0.1	−1.7/−1.6	3.3	
BLYP	0.1	0.1	−1.7/−1.6	3.3	
B3LYP	0.1	0.1	−1.7/−1.7	3.4	
BHLYP	0.0	0.0	−1.8/−1.7	3.4	3.5
B-60LYP	0.0	0.0	−1.8/−1.7	3.4	
B-70LYP	0.0	0.0	−1.8/−1.7	3.4	
Exp.[d]	0.0		−1.75	3.6	
Exp.[e]	0.1		−1.94	3.9	
H(6)					
dist. X-ray[b] 3.39 Å					
BP86	0.0	0.0	−2.0/−1.8	3.8	
BLYP	0.0	0.0	−1.9/−1.8	3.8	
B3LYP	0.0	0.0	−2.0/−1.9	3.9	
BHLYP	0.0	0.0	−2.0/−1.9	3.9	4.1
B-60LYP	0.0	0.0	−2.0/−1.9	3.9	

Table 4 continued

	A_{iso}	A^{FC}	$A_{11}^{\mathrm{dip}}/A_{22}^{\mathrm{dip}}$	A_{33}^{dip}	A'^{a}
B-70LYP	−0.1	−0.1	−2.0/−1.9	3.9	
dist. ENDOR[c] 3.56 Å					
BP86	0.0	0.0	−1.7/−1.6	3.3	
BLYP	0.0	0.0	−1.7/−1.6	3.3	
B3LYP	0.0	0.0	−1.7/−1.7	3.4	
BHLYP	0.0	0.0	−1.7/−1.7	3.4	3.5
B-60LYP	0.0	0.0	−1.7/−1.7	3.4	
B-70LYP	0.0	0.0	−1.7/−1.7	3.4	
Exp.[d]	0.0		−1.75	3.6	
Exp.[e]	0.1		−1.99	4.0	

[a] Anisotropic term A' derived from the point-dipole approximation: $A' = \frac{g_e \beta_e g_N \beta_N}{h r^3} \rho (3\cos^2\delta - 1)$ $[MHz]$, where g_e and g_N are the electron and nuclear g-values, ρ is the spin density at the manganese atom, δ is the angle between the applied field and the direction of the hydrogen bond, and r is the distance Mn–H in Å

[b] H-Mn distance with optmized imidazole proton positions (see Sect. 2)

[c] Mn–L bond lengths adjusted to reproduce ENDOR Mn–H distances (see Sect. 2)

[d] From 95 GHz ENDOR; accuracy ±0.1 MHz [9]

[e] From 95 GHz ENDOR; accuracy ±0.04 MHz [11]

Table 5 Computed and experimental ^{17}O HFC tensors (in MHz) of $[\mathrm{Mn(H_2O)_6}]^{2+}$

	A_{iso}	A^{FC}	A_{11}^{dip}	$A_{22}^{\mathrm{dip}}/A_{33}^{\mathrm{dip}}$	$½(A_{22}^{\mathrm{dip}} + A_{33}^{\mathrm{dip}})$
BP86	−10.9	−10.9	−2.0	0.3 / 1.7	1.0
BLYP	−12.5	−12.5	−2.1	0.3 / 1.9	1.1
B3LYP	−10.8	−10.8	−2.2	0.5 / 1.7	1.1
BHLYP	−10.1	−10.1	−2.2	0.6 / 1.6	1.1
B-60LYP	−9.8	−9.8	−2.3	0.7 / 1.6	1.2
B-70LYP	−9.6	−9.6	−2.3	0.7 / 1.6	1.2
B-80LYP	−9.5	−9.5	−2.3	0.7 / 1.6	1.2
B-90LYP	−9.3	−9.3	−2.3	0.7 / 1.6	1.2
B-95LYP	−9.3	−9.3	−2.3	0.7 / 1.6	1.2
Neese[a]	−11.3	−11.3	−2.2	0.5 / 1.7	1.1
Exp.[b]	−7.5	−7.5	−2.0	1.0 / 1.0	1.0

[a] DFT calculations with ORCA (B3LYP, [CP(PPP)] for Mn, EPR-II for ligand atoms) [50]

[b] Frozen solution 95 GHz ENDOR study of Ref. [50]

elongation of the Mn–L distances to reproduce hydrogen positions deduced from ENDOR spectra [9] (cf. see Sect. 2). Experiments indicate approximately axial symmetry for the proton HFC tensors. This is confirmed by the calculations. SO corrections are negligible for the proton HFC tensors and are thus not provided in the table.

Starting with the anisotropic parts of the six ^{1}H HFC tensors studied, we see very little dependence on the functional and rather good agreement with experiment, including the trends for the different H_2O proton locations. This suggests that the anisotropic tensor components are dominated by the direct dipolar interaction with the metal-centered spin density. Then the point-dipolar approximation should work well, as does seem to be the case (see Table 4). Indeed, agreement between ENDOR-derived and computed Mn–H distances is essentially perfect for water protons H(1)–H(3), whereas estimates based on ENDOR appear to overestimate the remaining distances by about 0.2 Å.

Turning to the more difficult A_{iso} of the water protons, we see that the diminishing spin delocalization onto the ligands with increasing exact-exchange admixture reduces the isotropic hyperfine couplings and thereby brings the computations into better agreement with experiment. Changes above 50% exact exchange tend to be small. For H(4), use of the larger ENDOR-derived Mn–H distance would interestingly lead to a much larger A_{iso} (Mulliken spin densities on H(4) are also consistently about twice the value for the optimized structure, for all functionals). It is clear, however, that in this case the shorter, optimized distance and the lower A_{iso} values are to be preferred. The optimized distance agrees also better with ^{2}D ENDOR measurements on a concanavalin A preparation with deuterated ligands (d(Mn–D)=3.08 Å) [9].

The two histidine protons H(5) and H(6) exhibit an almost purely dipolar tensor [9], as is confirmed by the computations (so is the magnetic equivalence of the two protons). Here the dipolar tensor depends very slightly more on the functional than for H(1)–H(4). The optimized Mn–H(5) and Mn–H(6) distances agree much better with crystallographic data [11] (Mn–H(5) = 3.41 Å, Mn–H(6) = 3.44 Å) than with the larger ENDOR-derived values.

3.5 ^{17}O hyperfine coupling constants

To predict the ^{17}O hyperfine interaction of the water ligands and the coordinated amino acids, different DFT methods were first validated on the Mn^{2+} hexaquo complex, for which high-field ENDOR data are available (Table 5) [50]. The sign of the experimentally determined $^{17}\mathrm{O}\,A_{\mathrm{iso}}$ could be confirmed, but the calculations show a notable deviation from axiality. The isotropic coupling is slightly overestimated in the DFT calculations and shows the best agreement with experiment at relatively large exact exchange-admixture (>50%). The anisotropic part does not depend much on the functional and is exactly reproduced with the GGA functional BP86.

Following these results for $[\mathrm{Mn(H_2O)_6}]^{2+}$, Table 6 compares the ^{17}O HFCs for the two different Concanavalin A structures (cf. Sect. 2) for the BP86 and B-60LYP functionals. As already observed for the Mn^{2+} aquo complex, there is not much variation for the different components of the hyperfine coupling tensor of the oxygen atoms of the amino acid ligands O(1), O(2) and O(3) with different functionals,

Table 6 Computed and experimental ^{14}N and ^{17}O HFC tensors (in MHz) in the concanavalin A model

L	d(Mn–L)		A_{iso}	A^{FC}	A_{11}^{dip}	A_{22}^{dip}	A_{33}^{dip}
O(1)	dist. X-ray[a]	BP86	−8.7	−8.7	−3.3	1.3	2.0
	2.15 Å	B-60LYP	−8.8	−8.8	−2.7	1.1	1.6
	dist. ENDOR[b]	BP86	−7.8	−7.8	−3.7	1.4	2.3
	2.15 Å	B-60LYP	−8.0	−8.0	−2.6	1.1	1.5
O(2)	dist. X-ray[a]	BP86	−9.2	−9.2	−2.5	1.0	1.5
	2.17 Å	B-60LYP	−9.3	−9.3	−2.6	1.2	1.4
	dist. ENDOR[b]	BP86	−8.7	−8.7	−2.5	1.0	1.5
	2.17 Å	B-60LYP	−8.9	−8.9	−2.6	1.2	1.4
O(3)	dist. X-ray[a]	BP86	−7.5	−7.5	−1.8	0.4	1.4
	2.19 Å	B-60LYP	−7.9	−7.9	−2.1	0.7	1.3
	dist. ENDOR[b]	BP86	−6.1	−6.1	−1.6	0.3	1.3
	2.15 Å	B-60LYP	−7.1	−7.1	−1.9	0.6	1.3
O(4)	dist. X-ray[a]	BP86	−22.8	−22.8	−1.1	0.0	1.0
	2.18 Å	B-60LYP	−12.5	−12.5	−2.0	0.6	1.4
	dist. ENDOR[b]	BP86	−21.2	−21.2	−1.0	0.0	1.1
	2.16 Å	B-60LYP	−11.7	−11.7	−2.0	0.6	1.4
O(5)	dist. X-ray[a]	BP86	−14.7	−14.7	−1.4	0.3	1.1
	2.26 Å	B-60LYP	−10.3	−10.3	−2.0	0.7	1.3
	dist. ENDOR[b]	BP86	−11.6	−11.6	−1.4	0.5	0.9
	2.41 Å	B-60LYP	−7.9	−7.9	−1.8	0.7	1.1
N(1)	dist. X-ray[a]	BP86	4.0	4.0	−0.7	−0.6	1.4
	2.23 Å	B-60LYP	3.9	3.9	−0.7	−0.6	1.3
	dist. ENDOR[b]	BP86	4.1	4.1	−0.7	−0.6	1.3
	2.44 Å	B-60LYP	3.6	3.6	−0.6	−0.5	1.1

[a] H–Mn distance with optmized imidazole proton positions (see Sect. 2)

[b] Mn-L bond lengths adjusted to reproduce ENDOR Mn-H distances (see Sect. 2)

even though the Mulliken spin densities have different signs for O(2) and O(3) for the different functionals (negative for BP86, positive for B-60LYP, see Table 1). The choice of the model (X-ray vs. ENDOR-based distances, cf. above) also affects the hyperfine couplings of the amino-acid oxygen atoms very little.

In contrast to O(1)–O(3), the exchange-correlation functional influences the HFCs much more for the water oxygen atoms O(4) and O(5), in particular for the isotropic value. Here the substantial differences between the X-ray- and ENDOR-derived Mn-O distances also lead to appreciable variations in the computed HFC tensors.

Table 6 also provides results for nitrogen atom N(1) of the imidazole ligand. In spite of a strong influence of exact-exchange admixture on the Mulliken spin density (cf. Table 1), even the isotropic nitrogen hyperfine coupling constant is affected very little.

4 Conclusions

We have used the structurally and EPR/ENDOR-spectroscopically well-characterized manganese site in the saccharide-binding protein concanavalin A to evaluate (a) the performance of different DFT exchange-correlation potentials for the calculation of spin-density distribution and metal/ligand hyperfine parameters in biological manganese sites, and (b) the validity of the point-dipole approximation in estimating proton positions on coordinated protein residues and water molecules from ENDOR data.

Isotropic hyperfine couplings on both metal and the ligand protons are best reproduced when the hybrid functional exhibits about 50% or more exact-exchange admixture. This is consistent with previous results for both very early 3d metal centers (e.g. V^{IV} complexes [51,52]) and very late metals (e.g. for Cu^{II} systems [47]). Notably, spin contamination is no problem with larger exact-exchange admixture but even diminishes, due to decreased metal–ligand covalency. Spin-orbit contributions to the metal hyperfine tensor have been found to be small, consistent with the high-spin d^5 electronic characteristics.

Anisotropic ^{1}H HFCs are relatively insensitive to the exact-exchange admixture, demonstrating that they are dominated by the large metal-centered spin density. This helps to justify the point-dipole approximation used to estimate hydrogen-atom positions from dipolar HFCs determined in ENDOR spectra. The ENDOR-derived distances agree well with optimized Mn–H distances for water protons H(1)–H(3) but overestimate the experimental and computed values by about 0.2 Å for the remaining protons. The ^{17}O HFCs for the oxygen atoms directly bonded to the manganese center in concanavalin A were predicted based on prior method validation for the $[\mathrm{Mn}(\mathrm{H}_2^{17}\mathrm{O})_6]^{2+}$ complex.

Acknowledgments We are grateful to R. Reviakine for technical assistance. S.S. thanks Fonds der Chemischen Industrie for a doctoral scholarship.

References

1. Kalb AJ, Habash J, Hunter NS, Price HJ, Raftery J, Helliwell JR (2000) Metal Ions Bioll Systems 37:279–304
2. Greer J, Kaufman HW, Kalb AJ (1970) J Mol Biol 48:365–366
3. Sumner JB, Howell SF (1936) J Bacter 32:227–237
4. Shoham M, Kalb AJ, Pecht I (1973) Biochemistry 12:1914–1917
5. Weis WI, Drickamer K (1996) Annu Rev Biochem 65:441–473
6. Deacon A, Gleichmann T, Kalb AJ, Price H, Raftery J, Bradbrook G, Yariv J, Helliwell JR (1997) J Chem Soc, Faraday Trans 93:4305–4312
7. Meirovitch E, Luz Z, Kalb AJ (1974) J Am Chem Soc 96:7542–7546
8. Meirovitch E, Luz Z, Kalb AJ (1974) J Am Chem Soc 96:7538–7542
9. Manikandan P, Carmieli R, Shane T, Kalb AJ, Goldfarb D (2000) J Am Chem Soc 122:3488–3494
10. Metz H, Kuchler J, Bottcher R, Windsch W (1982) Chem Phys Lett 89:351–355
11. Carmieli R, Manikandan P, Kalb AJ, Goldfarb D (2001) J Am Chem Soc 123:12438
12. Harriman JE (1978) Theoretical foundations of electron spin resonance. Academic Press, New York
13. Abragam A, Bleaney B (1970) Electron paramagnetic resonance of transition ions. Clarendon Press, Oxford
14. Atherton NM (1993) Principles of electron spin resonance. Prentice-Hall, New York
15. Weil JA, Bolton JR, Wertz JE (1994) Electron paramagnetic resonance: elementary theory and practical applications. Willey, New York
16. McGarvey BR (1966) Transition Metal Chem (New York) 3:89–201
17. Mabbs FE, Collison D (1992) Electron paramagnetic resonance of d transition metal compounds. Elsevier, Amsterdam
18. Malkina OL, Vaara J, Schimmelpfennig B, Munzarova M, Malkin VG, Kaupp M (2000) J Am Chem Soc 122:9206–9218
19. Kaupp M, Reviakine R, Malkina OL, Arbuznikov A, Schimmelpfennig B, Malkin VG (2002) J Comp Chem 23:794–803
20. Schreckenbach G, Ziegler T (1997) J Phys Chem A 101:3388–3399
21. Neese F (2001) J Chem Phys 115:11080–11096
22. Arbuznikov A, Vaara J, Kaupp M (2004) J Chem Phys 120:2127–2139
23. Remenyi C, Reviakine R, Arbuznikov AV, Vaara J, Kaupp M (2004) J Phys Chem A 108:5026–5033
24. Neese F (2003) J Chem Phys 118:3939–3948
25. Ahlrichs R, Bär M, Häser M, Horn H, Kölmel C (1989) Chem Phys Lett 162:165–169
26. Stephens PJ, Devlin FJ, Chabalowski CF, Frisch MJ (1994) J Phys Chem 98
27. Becke AD (1993) J Chem Phys 98:5648
28. Schäfer A, Horn H, Ahlrichs R (1992) J Chem Phys 97:2571–2577
29. Frisch MJ, Trucks GW, Schlegel HB, Scuseria GE, Robb MA, Cheeseman JR, Montgomery JA Jr, Vreven T, Kudin KN, Burant JC, Millam JM, Iyengar SS, Tomasi J, Barone V, Mennucci B, Cossi M, Scalmani G, Rega N, Petersson GA, Nakatsuji H, Hada M, Ehara M, Toyota K, Fukuda R, Hasegawa J, Ishida M, Nakajima T, Honda Y, Kitao O, Nakai H, Klene M, Li X, Knox JE, Hratchian HP, Cross JB, Bakken V, Adamo C, Jaramillo J, Gomperts R, Stratmann RE, Yazyev O, Austin AJ, Cammi R, Pomelli C, Ochterski JW, Ayala PY, Morokuma K, Voth GA, Salvador P, Dannenberg JJ, Zakrzewski VG, Dapprich S, Daniels AD, Strain MC, Farkas O, Malick DK, Rabuck AD, Raghavachari K, Foresman JB, Ortiz JV, Cui Q, Baboul AG, Clifford S, Cioslowski J, Stefanov BB, Liu G, Liashenko A, Piskorz P, Komaromi I, Martin RL, Fox DJ, Keith T, Al-Laham MA, Peng CY, Nanayakkara A, Challacombe M, Gill PMW, Johnson B, Chen W, Wong MW, Gonzalez C, Pople JA (2004) Gaussian 03, Revision C.02: Gaussian, Wallingford
30. Munzarová M, Kubácek P, Kaupp M (2000) J Am Chem Soc 122:11900
31. Munzarová M, Kaupp M (1999) J Phys Chem A 103:9966–9983
32. Kutzelnigg W, Fleischer U, Schindler M (1990) In: Diehl P, Fluck E, Günther H, Kosfeld R, Seelig J (eds) NMR basis principles and progress, vol 23. Springer, Berlin
33. Huzinaga S (1971) Ph D thesis. University of Alberta, Edmonton
34. Becke AD (1988) Phys Rev A 38:3098–3100
35. Perdew JP (1986) Phys Rev B 33:8822–8824
36. Lee C, Yang W, Parr RG (1988) Phys Rev B 37:785
37. Malkin VG, Malkina OL, Reviakine R, Arbouznikov AV, Kaupp M, Schimmelpfennig B, Malkin I, Helgaker T, Ruud K (2003) MAG-Respect, Version 1.2
38. Hess BA, Marian CM, Wahlgren U, Gropen O (1996) Chem Phys Lett 251:365
39. Schimmelpfennig B (1996) Ph.D. thesis: Stockholms Universitet, Sweden
40. Carmieli R, Manikandan P, Epel B, Kalb AJ, Schnegg A, Savitsky A, Moebius K, Goldfarb D (2003) Biochemistry 42:7863–7870
41. Goldfarb D, Arieli D (2004) Ann Rev Biophys Biomol Struct 33:441–468
42. Goldfarb D, Narasimhulu KV, Carmieli R (2005) Magn Reson Chem 43:S40–S50
43. Patchkovskii S, Ziegler T (1999) J Chem Phys 111:5730–5740
44. Solomon EI, Szilagyi RK, DeBeer George S, Basumallick L (2004) Chem Rev 104:419–458
45. Remenyi C, Kaupp M (2005) J Am Chem Soc 127:11399–11413
46. Ciofini I, Illas F, Adamo C (2004) J Chem Phys 120:3811–3816
47. Remenyi C, Reviakine R, Kaupp M (2007) J Phys Chem B 111:8290–8304
48. Malkin VG, Malkina OL, Casida ME, Salahub DR (1994) J Am Chem Soc 116:5898
49. Arieli D, Prisner TF, Hertel M, Goldfarb D (2004) Phys Chem Chem Phys 6:172–181
50. Baute D, Goldfarb D (2005) J Phys Chem A 109
51. Munzarová ML, Kaupp M (2001) J Phys Chem B 105:12644–12652
52. Remenyi C, Munzarova ML, Kaupp M (2005) J Phys Chem B 109:4227–4233